

# Photoluminescence Quenching Probes Spin Conversion and Exciton Dynamics in Thermally Activated Delayed Fluorescence Materials

Brett Yurash, Hajime Nakanotani, Yoann Olivier, David Beljonne, Chihaya Adachi, and Thuc-Quyen Nguyen\*

Fluorescent materials that efficiently convert triplet excitons into singlets through reverse intersystem crossing (RISC) rival the efficiencies of phosphorescent state-of-the-art organic light-emitting diodes. This upconversion process, a phenomenon known as thermally activated delayed fluorescence (TADF), is dictated by the rate of RISC, a material-dependent property that is challenging to determine experimentally. In this work, a new analytical model is developed which unambiguously determines the magnitude of RISC, as well as several other important photophysical parameters such as exciton diffusion coefficients and lengths, all from straightforward time-resolved photoluminescence measurements. From a detailed investigation of five TADF materials, important structure–property relationships are derived and a brominated derivative of 2,4,5,6-tetrakis(carbazol-9-yl)isophthalonitrile that has an exciton diffusion length of over 40 nm and whose excitons interconvert between the singlet and triplet states  $\approx 36$  times during one lifetime is identified.

In organic light-emitting diodes (OLEDs), due to the spin statistics of injected charges, roughly 75% of all molecular excitations in the emissive layer have triplet character with the remaining 25% being singlet. Thus, in order to achieve the ultimate device efficiency, emitter molecules must be able to transform both singlet excitons and triplet excitons into emitted photons. In 2009, OLEDs based on a new class of materials were demonstrated to be capable of efficiently


harvesting triplet excitons via reverse intersystem crossing (RISC), which is enabled in molecules with small singlet-triplet splitting energy ( $\Delta E_{ST}$ ).<sup>[1]</sup> The photoemission observed when a triplet exciton upconverts into a singlet exciton and then emits from the singlet state is known as thermally activated delayed fluorescence (TADF). Whereas commercially available OLEDs that currently rely on phosphorescence (PhOLEDs) require expensive heavy metals with a limited global supply, OLEDs based on TADF (TADF-OLEDs) are amenable to facile, scalable, and inexpensive synthetic routes.<sup>[2–4]</sup> Already some TADF-OLEDs have been shown to have an external quantum efficiency of over 20%, which is comparable to the best PhOLEDs and implies an internal quantum efficiency (IQE) of nearly 100%.<sup>[5,6]</sup>

Although there has been a significant theoretical and computational effort addressing the mechanistic aspects of RISC, the experimental determination of RISC has not been thoroughly revisited since the pioneering work of Berberan-Santos and co-workers.<sup>[7–10]</sup> The Berberan-Santos (B.-S.) method, which is the most frequently drawn upon model in the TADF literature, relies on two key assumptions: i) that the rate of intersystem crossing ( $k_{ISC}$ ) is significantly larger than the rate of RISC ( $k_{RISC}$ ) and ii) that the material of interest exhibits “strong” delayed fluorescence (see the Supporting Information for more details). As shown in this work, however, not all TADF materials meet these criteria. Furthermore, this method heavily depends on the accurate determination of  $k_{ISC}$ , which is not trivial. One of the commonly used methods to determine  $k_{ISC}$ , which involves triplet exciton quenching via oxygen, depends on criterion (ii) mentioned above.<sup>[11]</sup> Another commonly used method is predicated on the assumption that nonradiative decay from the singlet state is negligible, which is certainly not the case for all TADF materials, as shown in this work.<sup>[12,13]</sup> Although this condition is commonly satisfied at cryogenic temperatures, the subsequent value of  $k_{ISC}$  that is determined at these low temperatures will only apply to room temperature conditions if  $k_{ISC}$  and the rate of radiative decay from the singlet state are independent of temperature, which we find not to be true at least for the series of compounds investigated herein.

B. Yurash, Prof. T.-Q. Nguyen  
Department of Chemistry and Biochemistry  
University of California  
Santa Barbara, CA 93106, USA  
E-mail: quyen@chem.ucsb.edu

Prof. H. Nakanotani, Prof. C. Adachi  
Center for Organic Photonics and Electronics Research (OPERA)  
Kyushu University  
744 Motooka, Nishi, Fukuoka, 819-0395 Japan

Dr. Y. Olivier, Prof. D. Beljonne  
Laboratory for Chemistry of Novel Materials  
University of Mons  
Place du Parc 20, B-7000 Mons, Belgium

 The ORCID identification number(s) for the author(s) of this article can be found under <https://doi.org/10.1002/adma.201804490>.

DOI: 10.1002/adma.201804490

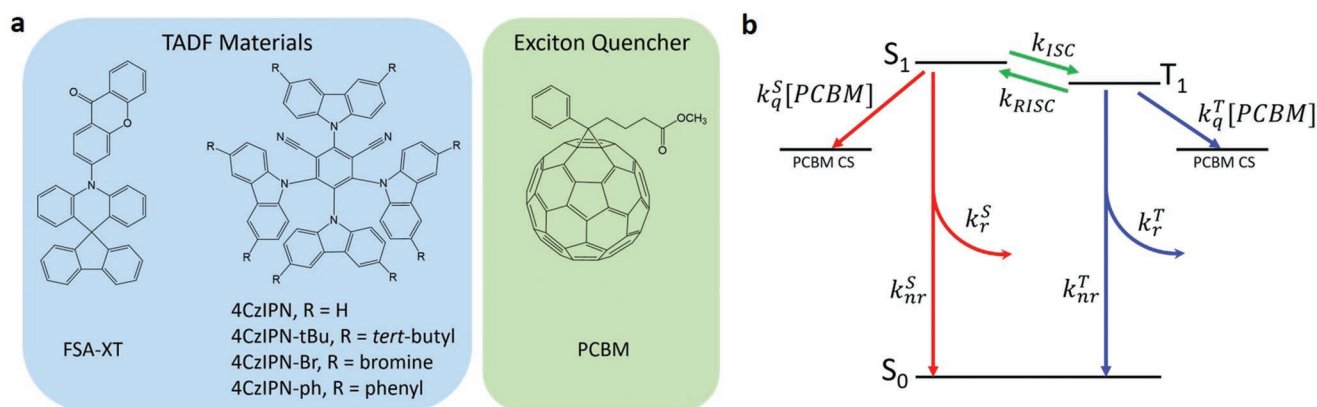


**Figure 1.** a) Chemical structure and names of the TADF materials studied herein and the exciton quencher, PCBM. b) Simplified Jablonski diagram showing the relevant excited-state transitions for a TADF material in the presence of an exciton quencher, i.e., PCBM.

In light of all of these considerations, a more robust and widely applicable method of determining  $k_{RISC}$  in TADF materials is highly desirable. In this work, we develop an analytical model that describes the time-dependent photoluminescence (PL) decay of TADF materials in the presence of an exciton quencher, i.e., [6,6]-phenyl  $C_{61}$  butyric acid methyl ester (PCBM). From just time-resolved data our analytical model is able to accurately determine not only the rate of RISC in TADF materials, but also the rate of ISC,  $\Delta E_{ST}$ , and the diffusivity of both singlet and triplet excitons. With this new analytical approach combined with complementary quantum-chemical calculations, we have managed to unravel the complex photo-physical properties of five TADF molecules in pristine films and in solution, namely, 3-(10*H*-spiro[acridine-9,9'-fluoren]-10-yl)-9*H*-xanthen-9-one (FSA-XT), 2,4,5,6-tetrakis(carbazol-9-yl)isophthalonitrile (4CzIPN), 2,4,5,6-tetrakis(3,6-di-*tert*-butylcarbazol-9-yl)isophthalonitrile (4CzIPN-tBu), 2,4,5,6-tetrakis(3,6-dibromocarbazol-9-yl)isophthalonitrile (4CzIPN-Br), and

2,4,5,6-tetrakis(3,6-diphenylcarbazol-9-yl)isophthalonitrile (4CzIPN-ph), which differ either in molecular architecture (FSA-XT vs 4CzIPN) or by the nature of their substituting moieties (4CzIPN and its derivatives) (Figure 1a).<sup>[5,14]</sup>

The molar absorptivity and photoluminescence of thin films of these materials are shown in Figure S1 in the Supporting Information. The 4CzIPN-related molecules are characterized by moderate molar absorptivities in the 400 nm region, which is attributed to a donor–acceptor (carbazole-dicyanobenzene)  $\pi \rightarrow \pi^*$  transition. The extremely weak molar absorptivity around 400 nm for FSA-XT is a direct consequence of the high degree of charge-transfer character in this optical transition. Density functional theory (DFT) calculations suggest this optical transition is the result of a donor–acceptor (acridine-xanthenone)  $\pi \rightarrow \pi^*$  transition with very little wavefunction overlap between the electron and hole. The overlaps between electron and hole densities computed in the attachment/detachment formalism,  $\phi_s$ , are listed in Table 1.<sup>[15]</sup> The calculated

**Table 1.** Summary of results.

	FSA-XT	4CzIPN	4CzIPN-tBu	4CzIPN-Br	4CzIPN-ph
$k_{p0}$ [ $s^{-1}$ ]	$3.2 \times 10^7$	$4.5 \times 10^7$	$5.1 \times 10^7$	$4.2 \times 10^8$	$6.7 \times 10^7$
$k_{ISC}$ [ $s^{-1}$ ]	$7.5 \times 10^6$	$2.6 \times 10^6$	$1.4 \times 10^6$	$2.5 \times 10^8$	$1.7 \times 10^7$
$k_{RISC}$ [ $s^{-1}$ ]	$1.4 \times 10^6$	$5.9 \times 10^5$	$6.5 \times 10^5$	$4.4 \times 10^6$	$1.1 \times 10^6$
$k_{d0}$ [ $s^{-1}$ ]	$1.0 \times 10^6$	$5.7 \times 10^5$	$6.3 \times 10^5$	$1.7 \times 10^6$	$8.3 \times 10^5$
Experimental $\Delta E_{ST}$ [meV]	21	43	57	18	39
Theoretical $\Delta E_{ST}$ [meV]	12	80	79	53	21
$V_{SOC}$ [meV] ISC/RISC	0.004/0.004	0.016/0.024	0.015/0.020	0.089/0.142	0.003/0.006
$\phi_s(S_1)/\phi_s(T_1)$	0.16/0.18	0.40/0.46	0.35/0.41	0.33/0.39	0.33/0.43
$D_{singlet}$ [ $cm^2 s^{-1}$ ]	$2.3 \times 10^{-6}$	$3.9 \times 10^{-6}$	$5.5 \times 10^{-6}$	$1.9 \times 10^{-5}$	$4.2 \times 10^{-6}$
$D_{triplet}$ [ $cm^2 s^{-1}$ ]	$3.3 \times 10^{-8}$	$7.3 \times 10^{-9}$	$1.2 \times 10^{-8}$	$1.2 \times 10^{-7}$	$4.8 \times 10^{-9}$
$E_a$ singlet diffusion [meV]	34	32	52	8	37
$E_a$ triplet diffusion [meV]	144	92	117	128	134
Solid-state PLQY	0.72	0.30	0.23	0.22	0.19
Wigner–Seitz radius, $r$ [nm]	0.52	0.65	0.75	0.73	0.78
$\bar{n}$	0.27	0.53	0.89	36.12	0.22

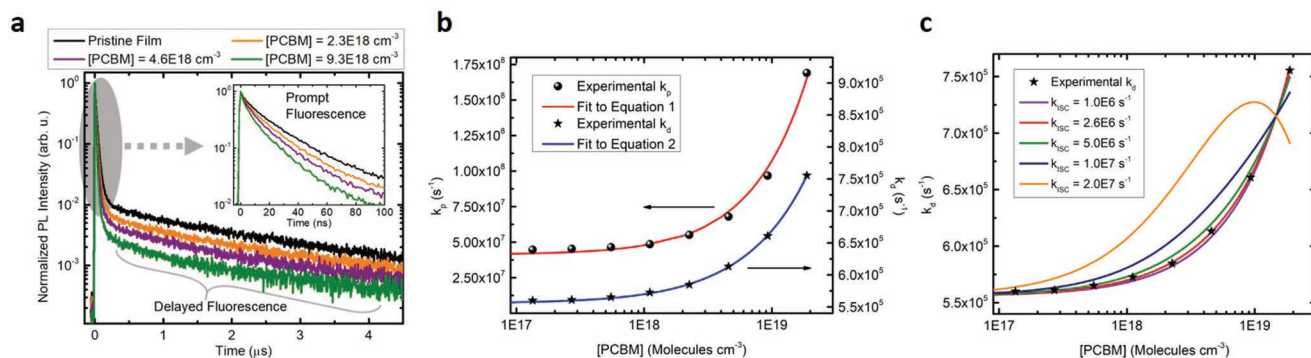


**Figure 2.** a) PL decay of 4CzIPN in the presence of various amounts of PCBM. b) Dependence of  $k_p$  and  $k_d$  on [PCBM] for 4CzIPN with fitting to the analytical model described in the text. c) Dependence of  $k_d$  on [PCBM] for 4CzIPN where arbitrary input values of  $k_{ISC}$  are fixed, resulting in  $k_q^T$  as the only fitting parameter.

equilibrium geometries (gas phase) of the materials corroborate these differences in molar absorptivity: the donor–acceptor dihedral angle in FSA-XT is  $\approx 90^\circ$ , whereas for the 4CzIPN-related molecules it resides closer to  $80^\circ$ .

Because the photoluminescence quantum yield (PLQY) of the emitter in any type of OLED is an extremely important parameter for maximizing luminance and external quantum efficiency, the solid-state PLQY was investigated for each material. Interestingly, we found that the total solid-state PLQY is inversely proportional to the size of the molecule and its Wigner–Seitz radius,  $r$ , a parameter that is commonly used to estimate average intermolecular distances (Figure S3, Supporting Information). Therefore, when designing new TADF materials it may be worthwhile to keep the size of the molecule as small as possible while also enabling them to pack densely in the solid state. Although a low molar absorptivity is often associated with a low PLQY, through our subsequent analysis of rate constants, we found that the high PLQY of FSA-XT can be mostly attributed to its small rate of nonradiative decay from the singlet state (Figure S12, Supporting Information).

equation.<sup>[16]</sup>  $k_{nr}^S$  and  $k_{nr}^T$  are the nonradiative rates of decay for singlets and triplets, respectively.  $k_r^S$  and  $k_r^T$  are the radiative rates of decay for singlets and triplets, respectively.  $k_{ISC}$  and  $k_{RISC}$  are the rates of intersystem crossing and reverse intersystem crossing, respectively. As shown in Figure 2a, the incorporation of small amounts of the exciton quencher, PCBM, into thin films results in a faster rate of decay for both the prompt ( $k_p$ ) and delayed ( $k_d$ ) components of the fluorescence decay of 4CzIPN.

As shown, numerical values obtained from fitting the PL decays of pristine (no quencher present) and blend (small amount of quencher) films can be fitted to an analytical model, resulting in the determination of  $k_{ISC}$ . The detailed kinetic model is presented in the Supporting Information, including the derivation for Equations (1)–(3), which are entirely original. Solution to the model yields i) the dependence of  $k_p$  on PCBM concentration, [PCBM] (Figure 2b, left axis)

$$k_p = k_{p0} + k_q^S [\text{PCBM}] \quad (1)$$

where  $k_{p0}$  is the rate of prompt fluorescence in a pristine film, and (ii) the rate of delayed fluorescence,  $k_d$ , as a function of PCBM concentration

$$k_d = \frac{1}{2} \left\{ \frac{k_{p0} + k_q^S [\text{PCBM}] + \left( \frac{k_{d0}^2 - k_{p0}k_{d0}}{k_{ISC} + k_{d0} - k_{p0}} \right) + k_q^T [\text{PCBM}] - \sqrt{\left[ \left( \frac{k_{d0}^2 - k_{p0}k_{d0}}{k_{ISC} + k_{d0} - k_{p0}} \right) + k_q^T [\text{PCBM}] - k_{p0} - k_q^S [\text{PCBM}] \right]^2 + 4 \times k_{ISC} \times \left( \frac{k_{d0}^2 - k_{p0}k_{d0}}{k_{ISC} + k_{d0} - k_{p0}} \right)}}{2} \right\} \quad (2)$$

All of the possible excited-state transitions that can occur in a thin-film of a TADF material while in the presence of a small amount of exciton quencher (PCBM) are shown in the simplified energy diagram of Figure 1b.  $S_1$  and  $T_1$  represent the lowest energy singlet and triplet excited states, respectively. The charge-separated (CS) state to PCBM is included to reflect the possibility of singlet and triplet excitons quenching via photoinduced electron transfer, which is expected to be favorable due to PCBM's strong electron affinity.  $k_q^S$  and  $k_q^T$  are the bimolecular quenching constants for singlets and triplets, respectively, and are related to diffusion coefficients via the Smoluchowski

where  $k_{d0}$  is the rate of delayed fluorescence in a pristine film.  $k_p$  and  $k_d$  are readily obtained from a biexponential fit to the fluorescence decay. First,  $k_q^S$  is obtained from a fit to Equation (1) as shown in Figure 2b (red line, left axis) for 4CzIPN. Then, Equation (2) is fitted to a plot of  $k_d$  versus [PCBM] as also shown in Figure 2b (blue line, right axis), where the only fitting parameters are  $k_{ISC}$  and  $k_q^T$ . Good agreement between the analytical model and experimental data cannot be achieved for other values of  $k_{ISC}$  (Figure 2c). When pyrene was used as an exciton quencher, instead of PCBM, nearly identical values were obtained (Figure S7, Supporting Information), demonstrating

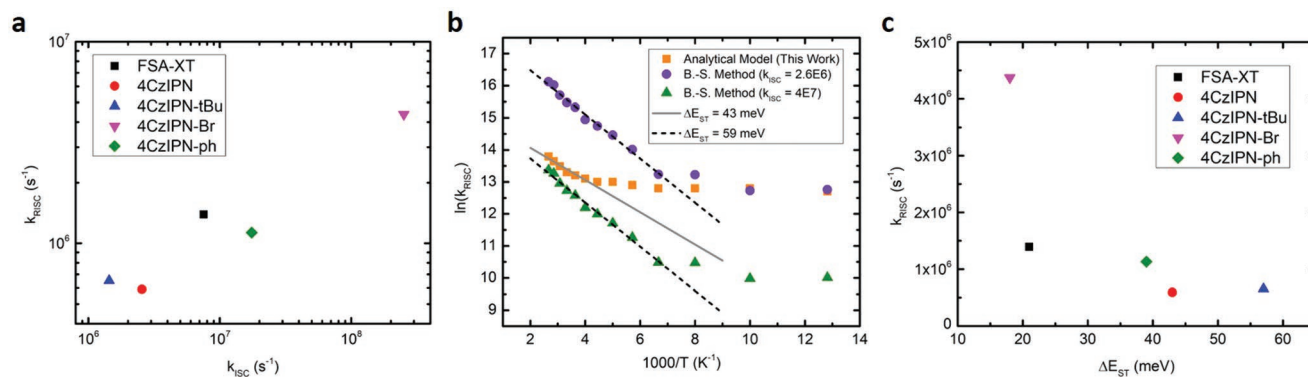


**Figure 3.** a) Results of the analytical model at room temperature. b) Arrhenius plot of  $k_{\text{RISC}}$  for 4CzIPN. The orange squares represent the results obtained from PL quenching and the analytical model described in this work. The green triangles and purple circles were calculated using the Berberan-Santos (B.-S.) method where different values of  $k_{\text{ISC}}$  were chosen for reasons described in the main text. c) Plotted values of  $k_{\text{RISC}}$  (at room temperature) and  $\Delta E_{\text{ST}}$  for each of the five TADF materials as determined by temperature-dependent PL quenching experiments.

the versatility of this analytical model. Once a value of  $k_{\text{ISC}}$  is obtained, the following equation is used to determine  $k_{\text{RISC}}$  for that material

$$k_{\text{RISC}} = \frac{k_{\text{d0}}^2 - k_{\text{p0}}k_{\text{d0}}}{k_{\text{ISC}} + k_{\text{d0}} - k_{\text{p0}}} \quad (3)$$

After implementing this technique for each of the five TADF materials, it becomes quite clear that there is a positive correlation between the rate of ISC and the rate of RISC (Figure 3a). This makes sense, because ISC and RISC likely proceed through the same mechanism, such that the main difference is simply the direction of the process and whether that means the initial state is higher or lower in energy than the final state. Thus, RISC is expected to be slower than ISC and a chemical modification that is designed to increase either of them will most likely end up increasing both. Although slow ISC may be incommensurable with fast RISC (a combination which would be ideal for TADF-OLEDs), the efficiency of ISC can be reduced if  $k_{\text{r}}^{\text{S}}$  is comparatively high. The design strategy for an ideal TADF material that emerges from this picture is to obtain a high  $k_{\text{RISC}}$  and high  $k_{\text{r}}^{\text{S}}$ . In terms of structure–property relationships, it is apparent that the inclusion of the heavy bromine atoms results in a large increase of both  $k_{\text{ISC}}$  and  $k_{\text{RISC}}$ . This is clearly associated with the much larger  $S_1$ – $T_1$  spin–orbit coupling ( $V_{\text{SOC}}$ ) calculated for 4CzIPN-Br in comparison to the other compounds, an obvious result of the heavy atom effect (see Table 1). The addition of *t*-butyl groups to the 4CzIPN structure had a minimal impact on the rates of ISC and RISC, but phenyl substituents resulted in significantly increased spin conversion rates. It was found that FSA-XT, most likely on account of its very small  $\Delta E_{\text{ST}}$  (vide infra), undergoes faster spin conversion than 4CzIPN.

Next, we have also estimated the impact of molecular architecture and substitution on the spin–orbit coupling,  $V_{\text{SOC}}$ , mediating spin conversion; these calculations were performed on the basis of the  $S_1$  and  $T_1$  geometries, relevant for ISC and RISC, respectively (Table 1). In line with our previous findings,  $V_{\text{SOC}}$  is larger for compounds with greater differences between their  $S_1$  and  $T_1$   $\phi_{\text{S}}$  values.<sup>[9]</sup> However, the calculated  $V_{\text{SOC}}$  values alone are not enough to understand the experimentally

determined trend in spin interconversion magnitudes, which leads us to believe that there may be a significant dynamic component (rotations, vibrations, torsions, etc.) that contributes to  $k_{\text{ISC}}$  and  $k_{\text{RISC}}$ .

To test this hypothesis, we employed our analytical model to  $50 \times 10^{-6}$  M solutions of each TADF material in benzene at room temperature using pyrene as an exciton quencher (see the Supporting Information for more details). We found that  $k_{\text{ISC}}$  and  $k_{\text{RISC}}$  were significantly higher in solution for the 4CzIPN derivatives (Figure S19, Supporting Information). This is most likely attributable to the extent of donor–acceptor rotational freedom available to the molecules. Whereas in the solid-state these rotations may have prohibitively high energy barriers, in solution these rotations are expected to happen quickly and efficiently. Previous work has shown that these rotations allow a molecule to explore its configurational space until a geometry is reached which favors (R)ISC.<sup>[8,9,17]</sup> We suspect that the additional rotations afforded by the phenyl groups of 4CzIPN-ph are responsible for its relative increase in spin conversion rates compared to 4CzIPN. For FSA-XT in solution  $k_{\text{ISC}}$  was marginally higher than in the solid-state and  $k_{\text{RISC}}$  was actually found to be smaller. We believe that this is a consequence of FSA-XT’s molecular geometry, such that (R)ISC would not benefit from additional rotational freedom and, in fact, suffers most probably due to the change in dielectric constant of the surrounding medium.<sup>[18]</sup> The enhancement of spin interconversion rates in solution and suppression of nonradiative decay pathways leads to a large increase in the average number of spin cycles,  $\bar{n}$ , each molecule experiences in the excited state, with  $\bar{n} = 1$  being defined as an  $S_1 \rightarrow T_1 \rightarrow S_1$  cycle. A value of  $\bar{n}$  less than 1 means that most of the generated excitons emit directly from the singlet state after absorption of light without ever undergoing ISC. For 4CzIPN-Br, we calculated  $\bar{n}$  to be 275 in benzene solution and 36 in the solid state. To the best of our knowledge, these are the largest values of  $\bar{n}$  reported in the literature for any TADF material (the highest values of  $\bar{n}$  that we could find ranged between 10 and 15).<sup>[10,11,19]</sup>

After performing photoluminescence quenching experiments at various temperatures, our analytical model was used to determine the temperature dependence of RISC, and, hence,  $\Delta E_{\text{ST}}$ . The orange squares in Figure 3b show the data obtained



for 4CzIPN after using our analytical model, where the slope of the solid gray line is proportional to the activation energy for RISC ( $\Delta E_{ST}$ ) in 4CzIPN. Note how at low temperatures  $k_{RISC}$  becomes much less temperature dependent, indicating a transition to a regime dominated by quantum mechanical tunneling.<sup>[20]</sup>

Figure 3b also shows the results for 4CzIPN when the Berberan-Santos method is used.<sup>[10]</sup> In that method, the magnitude of  $k_{RISC}$  is inversely proportional to the magnitude of  $k_{ISC}$ , and, therefore, an accurate determination of  $k_{RISC}$  is predicated on the accurate determination of  $k_{ISC}$ . Additionally, it is assumed that  $k_{ISC}$  is independent of temperature. As shown in Figure S10 (Supporting Information), we find  $k_{ISC}$  to be mildly temperature dependent. It is also worth mentioning that the Berberan-Santos method is only valid for materials that exhibit strong delayed fluorescence ( $\bar{n} \geq 4$ ) and that 4CzIPN does not meet this requirement ( $\bar{n} = 0.53$ ). Two vastly different values of  $k_{ISC}$  were chosen for the Berberan-Santos method of analysis:  $2.6 \times 10^6 \text{ s}^{-1}$  (purple circles) which is the value determined in this work at room temperature, and  $4.0 \times 10^7 \text{ s}^{-1}$  (green triangles) which is the value reported elsewhere in the literature for 4CzIPN.<sup>[5,19]</sup> In the first case, we find that  $k_{RISC}$  at room temperature ( $5.3 \times 10^6 \text{ s}^{-1}$ ) is larger than  $k_{ISC}$ , which is thermodynamically unreasonable. In the second case, the calculated value of  $k_{RISC}$  at room temperature ( $3.4 \times 10^5 \text{ s}^{-1}$ ) is within reasonable agreement to our value ( $5.9 \times 10^5 \text{ s}^{-1}$ ), but the ratio  $k_{ISC}/k_{RISC}$  is far off from what is obtained with our refined model (and also supported by recent computational efforts).<sup>[9]</sup> This highlights how the Berberan-Santos method can be less accurate for some TADF materials in regard to the magnitudes of  $k_{ISC}$  and  $k_{RISC}$ . For several of the materials we encountered difficulties extracting  $\Delta E_{ST}$  using the Berberan-Santos method (e.g., non-linear Arrhenius plots around room temperature), but never had issues using our model (Figure S17, Supporting Information). As shown in Figure 3c, we find that the rate of RISC is inversely proportional to  $\Delta E_{ST}$ , just as expected.

Reasonable agreement is found between measured and calculated singlet-triplet exchange energies. Both experiment and theory yield the largest  $\Delta E_{ST}$  values for 4CzIPN and 4CzIPN-tBu, in line with the largest  $\phi_S$  in their  $T_1$  and  $S_1$  excited-state wavefunctions suggesting an increased admixture of localized excitations in comparison to the other compounds.

For 4CzIPN-Br, the decrease in  $\Delta E_{ST}$  compared to 4CzIPN is induced by the presence of the electroactive bromine groups at the periphery of the carbazole units, which further separate away the hole from the electron density resulting in a more pronounced charge-transfer character. As expected, FSA-XT exhibits the lowest computed  $\Delta E_{ST}$  due to the  $\approx 90^\circ$  dihedral angle between donor and acceptor moieties, which also confers a high degree of CT character (small  $\phi_S$ ). In contrast to experiments, however, our calculations predict a surprisingly low  $\Delta E_{ST}$  value for 4CzIPN-Ph. Close inspection of the wavefunctions shows a partial delocalization of the hole electronic density into the outer phenyl rings, which enhances its CT character and thus reduces  $\Delta E_{ST}$ . The fact that comparable values are, instead, measured for 4CzIPN and 4CzIPN-Ph suggests that, likely because of steric conformational effects in the solid state, the phenyl rings are relatively decoupled from the core of the molecule in 4CzIPN-Ph.

Because singlet and triplet exciton diffusion appear as fitting parameters of our analytical model, we independently evaluated these parameters using a Monte Carlo simulation of exciton diffusion (see the Supporting Information for more details).<sup>[22]</sup> We were also motivated to study exciton diffusion, because very little is known about exciton diffusion in TADF materials. To the best of our knowledge, there has been only one other report concerning the measurement of exciton diffusion in a TADF material.<sup>[21]</sup> Very good agreement is found between the Monte Carlo simulation and results from the analytical model—within 17% for 4CzIPN.

The 3D singlet and triplet exciton diffusion lengths obtained for the five molecules are shown in Figure 4a. These values reflect how far a singlet or triplet exciton travels during its lifetime, excluding the possibility of RISC. Singlet exciton diffusion lengths seem to correlate inversely with molecular size, ranging from 7.9 nm (4CzIPN) to as short as 2.4 nm (4CzIPN-ph). Despite triplet excitons having a much longer lifetime than singlet excitons, they tend to diffuse over smaller distances owing to their relatively small diffusion coefficients (around 2 orders of magnitude less than singlet exciton diffusion coefficients). This is not surprising, given that nonluminescent triplet excitons are limited to Dexter energy transfer, whereas singlet excitons are expected to diffuse primarily via a Förster resonant energy transfer mechanism. Aside from

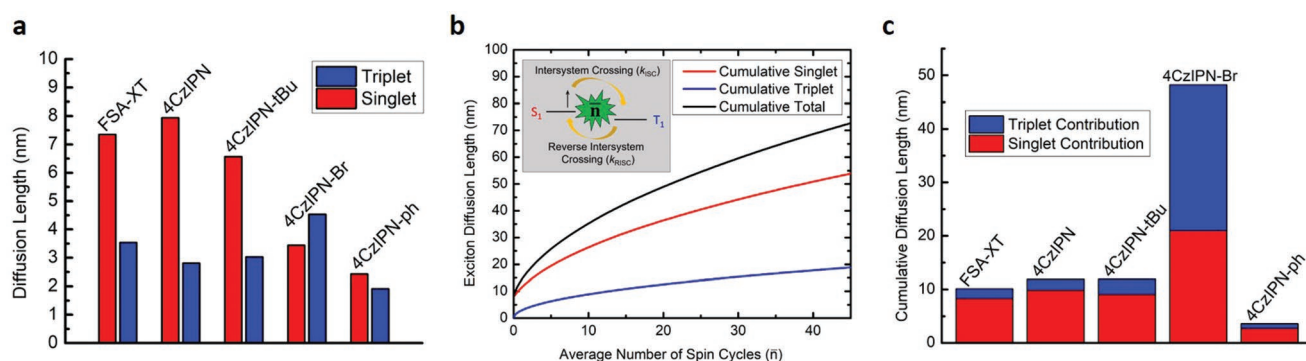


**Figure 4.** a) Singlet and triplet exciton diffusion lengths for one occurrence of the singlet or triplet excited state, respectively, at room temperature. b) Theoretical demonstration of how the extent of spin cycling affects the cumulative exciton diffusion length. c) Cumulative exciton diffusion lengths at room temperature where the effect of spin cycling has been taken into account.

4CzIPN-Br, the triplet exciton diffusion coefficients also scale inversely with the size of the molecule. A notable exception to the trend is 4CzIPN-Br, whose peripheral bromine atoms pulls the hole density toward the outer region of the molecule, likely improving intermolecular electronic interactions allowing for potential energy transfer via the Dexter (i.e., orbital overlap-driven) mechanism. A close examination of the experimentally determined rates of exciton diffusion indicates that, for singlet diffusion, the short-range Dexter mechanism of exciton transport is actually competitive with the longer-range Förster mechanism (Figure S16, Supporting Information). The observed correlation between exciton diffusion properties and molecular size can be simply understood by considering that larger molecules require longer hop sizes for exciton diffusion to occur (from a center-of-mass perspective), and both Förster and Dexter energy transfer efficiencies rapidly decline with increasing hop distances.

In order to grasp how far an exciton may diffuse during its entire lifetime (which we call the cumulative exciton diffusion length), the interconversion between the singlet and triplet states, i.e., spin cycling ( $\bar{n}$ ), must be accounted for. Figure 4b shows how exciton diffusion is expected to change with increasing spin cycling. (The diffusion coefficients and lifetimes of 4CzIPN are used in Figure 4b for purely demonstrative purposes.) Spin cycling has a rather small effect on the cumulative exciton diffusion length for most of the materials studied herein (Figure 4c) due to the low extent of spin cycling (Table 1). However, a notable exception is 4CzIPN-Br, whose high degree of spin cycling results in a dramatically increased cumulative exciton diffusion length (48.2 nm). This number appears to be exceptionally high in comparison to other materials exhibiting disordered thin film morphologies, such as certain  $\pi$ -conjugated polymers and small molecules, for which exciton diffusion lengths up to maximum 15 nm are usually reported.<sup>[23]</sup>

The temperature-dependent results of the analytical model conveniently enabled us to investigate the temperature dependence of exciton diffusion. Both triplet and singlet exciton diffusion appear to be thermally activated processes, although the activation energy tends to be higher for triplets (92 meV, 4CzIPN) than for singlets (32 meV, 4CzIPN). For the 4CzIPN derivatives, the activation energy for triplet diffusion again scales approximately with molecular size. At lower temperatures, exciton diffusion becomes weakly temperature dependent, an indication that transport has switched from a thermally activated hopping regime to a quantum mechanical tunneling regime. The temperature at which this transition occurs was found to be  $\approx 225$ – $250$  K for both singlet and triplet diffusion. This transition temperature has been shown to be strongly influenced by the relative degree of energetic disorder, where more ordered systems require less thermal energy to achieve thermally activated hopping transport. Small molecule and polymer organic semiconductors typically have a transition temperature below 150 K.<sup>[24–27]</sup> This would suggest that the TADF materials investigated in this work have a relatively large amount of disorder. Alternatively, the measured activation energy could, at least partly, stem from the intra- and inter-molecular structural reorganization as the excitons hop between molecules.<sup>[28]</sup> We are currently pursuing quantum-chemical modeling studies to disentangle these two contributions.

In this work, we develop an analytical model based on photoluminescence quenching, which is capable of unambiguously determining many of the crucial excited-state rate constants in TADF materials, both in solution and solid films. The assumptions upon which this model rests are far less restrictive than other methods used in the community, representing significant progress toward the accurate determination of  $k_{\text{ISC}}$  and  $k_{\text{RISC}}$ . Additionally, this experimental method enables the simultaneous measurement of the diffusion length for both singlet and triplet excitons, presenting a unique opportunity to investigate the different mechanisms of exciton diffusion without having to prepare separate samples or use more than one experimental technique. Using this method on five different TADF materials, we have gathered important insight on structure-function relationships. We have found that: i) heavy atoms (i.e., bromine) dramatically increase  $k_{\text{ISC}}$  and  $k_{\text{RISC}}$  while also reducing  $\Delta E_{\text{ST}}$ , ii) rotations about the donor and acceptor moieties heavily influence the dynamics of TADF, iii) the extent of spin cycling,  $\bar{n}$ , substantially impacts exciton diffusion length, and iv) molecular size is strongly correlated with exciton diffusion properties as well as solid-state PLQY. It is worth remarking on the exceptional properties of 4CzIPN-Br (fast  $k_{\text{ISC}}$  and  $k_{\text{RISC}}$ , small  $\Delta E_{\text{ST}}$ , large  $\bar{n}$ , long exciton diffusion length, and reasonable oscillator strength), which, besides making it a really promising emitter for TADF OLEDs, also make it a potential candidate for: i) triplet sensitizing in triplet-triplet annihilation photon upconversion,<sup>[29,30]</sup> ii) the 3.5 generation/hyperfluorescent OLED devices where TADF materials act as assistant dopants from where singlet excitons upconverted from the triplet excited-state manifold follow a fast energy transfer toward narrow emission fluorescent dyes,<sup>[31,32]</sup> and iii) bilayer organic photovoltaics whose thicknesses (and consequently their ability to harvest photons) are typically limited by rather short exciton diffusion lengths.<sup>[33,34]</sup>

## Experimental Section

**Materials:** 2,4,5,6-Tetrakis(carbazol-9-yl)isophthalonitrile, 2,4,5,6-tetrakis(3,6-di-*tert*-butylcarbazol-9-yl)isophthalonitrile, 2,4,5,6-tetrakis(3,6-diphenylcarbazol-9-yl)isophthalonitrile, 2,4,5,6-tetrakis(3,6-dibromocarbazol-9-yl)isophthalonitrile, and 3-(10*H*-spiro[acridine-9,9'-fluoren]-10-yl)-9*H*-xanthen-9-one were synthesized and purified according to the general procedures described in the literature.<sup>[5,14,35]</sup> [6,6]-Phenyl C<sub>61</sub> butyric acid methyl ester was purchased from Solenne in 99.9% purity. Pyrene was purchased from Sigma-Aldrich in 98% purity.

**Sample Preparation:** Pristine films of the TADF materials were produced by dissolving the material in chloroform ( $\approx 10$  mg mL<sup>-1</sup>) and spin-casting onto a clean glass substrate. In order to produce blend films with a specific concentration of PCBM, small quantities of PCBM dissolved in chloroform (1 mg mL<sup>-1</sup>) were added to a solution of the TADF material (10 mg mL<sup>-1</sup>), also in chloroform, in the desired ratio and then spin-casted onto a clean glass substrate. All films prepared were  $\approx 100$  nm thick as determined by a profilometer (Ambios) and X-ray reflectivity (Rigaku SmartLab). Samples were prepared in an inert nitrogen atmosphere and promptly encapsulated using epoxy and another glass substrate to avoid exposure to oxygen during subsequent optical measurements. Temperature-dependent measurements were taken by mounting samples in a closed-cycle nitrogen cryostat, pumping to vacuum ( $\approx 10^{-5}$  Torr), and modulating the temperature with a LakeShore autotuning temperature controller (model 321). For our solution-phase studies all samples were prepared in an inert glovebox environment and

transferred to air-tight quartz cuvettes before being removed for optical measurements, thus excluding oxygen entirely.

**Density Functional Theory:** All of the ground state optimization has been carried out at the density functional theory level with Gaussian 09 using the PBE0 functional and the 6-31G(d,p) basis considering toluene as solvent ( $\epsilon = 2.3741$ ) within the integral equation formalism model polarizable continuum model (IEFPCM).<sup>[36]</sup> Excited state calculations have been performed at time-dependent DFT (TD-DFT) within the Tamm–Dancoff approximation (TDA) using the same functional, basis set and solvent model as for ground state geometry optimization.<sup>[37]</sup> The  $\phi_5$  values have been calculated using the NANCY\_EX software based on the hole and electron densities as computed in the attachment/detachment formalism.<sup>[8,15]</sup> The spin–orbit coupling calculations have been performed using the PBE0 functional and the double zeta polarized basis set (DZP) within the scalar approximation to zero-order regular approximation (ZORA) to the full Breit–Dirac relativistic equation as implemented in ADF 2016.101.<sup>[38–42]</sup>

**Optical Characterization:** Photoluminescence decay measurements were carried out using a time-correlated single photon counting (TCSPC) technique. Samples were excited with a Ti:sapphire laser (Coherent Mira 900) that has an  $\approx 200$  fs pulse width. An excitation wavelength of 400 nm was obtained by using a commercial optical harmonic generator (Inrad) that doubled the fundamental frequency of the Ti:sapphire laser. The repetition rate of the laser was reduced by a home-made acousto-optical pulse picker in order to prevent saturation of the chromophore. The detector used was a single photon avalanche diode manufactured by microphoton devices. For all measurements, the intensity of the laser was attenuated such that each pulse produced fewer than  $3 \times 10^{11}$  excitons  $\text{cm}^{-2}$  (corresponding to an energy density of 500 pJ  $\text{cm}^{-2}$ ). Steady-state PL spectra were obtained by using an Acton Research SPC-500 monochromator and a charge-coupled device camera (Princeton Instruments PIXIS: 400). For the steady-state temperature-dependent photoluminescence measurements a 400 nm continuous wave diode laser with constant power output was employed.

## Supporting Information

Supporting Information is available from the Wiley Online Library or from the author.

## Acknowledgements

This project was supported by the Department of the Navy, Office of Naval Research (Award No. N00014-14-1-0580). X-ray reflectivity measurements were conducted in the MRL Shared Experimental Facilities at UCSB. The MRL Shared Experimental Facilities were supported by the MRSEC Program of the NSF under Award No. DMR 1720256. The calculation work in Mons was supported by the Programme d'Excellence de la Région Wallonne (OPTI2MAT project), the European Union's Horizon 2020 research and innovation program under Grant Agreement No. 646176 (EXTMOS project), and FNRS-FRFC. Computational resources were provided by the Consortium des Équipements de Calcul Intensif (CÉCI), funded by the Fonds de la Recherche Scientifiques de Belgique (F.R.S.-FNRS) under Grant No. 2.5020.11 as well as the Tier-1 supercomputer of the Fédération Wallonie-Bruxelles, infrastructure funded by the Walloon Region under Grant Agreement n1117545. D.B. and Y.O. would like to acknowledge the Belgian National Fund for Scientific Research (FNRS/FRS) for financial support. D.B. is an FNRS Research Director. Y.O. acknowledges fruitful discussions with Prof. Luca Muccioli from the University of Bologna and Prof. Juan-Carlos Sancho-García from the University of Alicante. B.Y. performed all of the experimental measurements, ran the Monte Carlo simulations of exciton diffusion, conceived/developed the analytical model, and synthesized 4CzIPN-Br. The other four molecules were synthesized in the lab of C.A. and H.N. T.Q.N. and D.B. supervised the project.

## Conflict of Interest

The authors declare no conflict of interest.

## Keywords

exciton diffusion, intersystem crossing, photoluminescence quenching, spin cycling, thermally activated delayed fluorescence

Received: July 13, 2018  
Revised: September 5, 2018  
Published online:

- [1] A. Endo, M. Ogasawara, A. Takahashi, D. Yokoyama, Y. Kato, C. Adachi, *Adv. Mater.* **2009**, *21*, 4802.
- [2] Y. Tao, K. Yuan, T. Chen, P. Xu, H. Li, R. Chen, C. Zheng, L. Zhang, W. Huang, *Adv. Mater.* **2014**, *26*, 7931.
- [3] Z. Yang, Z. Mao, Z. Xie, Y. Zhang, S. Liu, J. Zhao, J. Xu, Z. Chi, M. P. Aldred, *Chem. Soc. Rev.* **2017**, *46*, 915.
- [4] C. Adachi, *Jpn. J. Appl. Phys.* **2014**, *53*, 060101.
- [5] H. Uoyama, K. Goushi, K. Shizu, H. Nomura, C. Adachi, *Nature* **2012**, *492*, 234.
- [6] H. Kaji, H. Suzuki, T. Fukushima, K. Shizu, K. Suzuki, S. Kubo, T. Komino, H. Oiwa, F. Suzuki, A. Wakamiya, Y. Murata, C. Adachi, *Nat. Commun.* **2015**, *6*, 8476.
- [7] J. Gibson, A. P. Monkman, T. J. Penfold, *ChemPhysChem* **2016**, *17*, 2956.
- [8] Y. Olivier, M. Moral, L. Muccioli, J.-C. Sancho-García, *J. Mater. Chem. C* **2017**, *5*, 5718.
- [9] Y. Olivier, B. Yurash, L. Muccioli, G. D'Avino, O. Mikhnenko, J. C. Sancho-García, C. Adachi, T.-Q. Nguyen, D. Beljonne, *Phys. Rev. Mater.* **2017**, *1*, 075602.
- [10] C. Baleizão, M. N. Berberan-Santos, *J. Chem. Phys.* **2007**, *126*, 204510.
- [11] F. B. Dias, T. J. Penfold, A. P. Monkman, *Methods Appl. Fluoresc.* **2017**, *5*, 012001.
- [12] X. Cai, X. Li, G. Xie, Z. He, K. Gao, K. Liu, D. Chen, Y. Cao, S.-J. Su, *Chem. Sci.* **2016**, *7*, 4264.
- [13] N. Turro, V. Ramamurthy, J. Scaiano, *Modern Molecular Photochemistry of Organic Molecules*, University Science Books, Sausalito, CA **2010**.
- [14] J. Lee, N. Aizawa, M. Numata, C. Adachi, T. Yasuda, *Adv. Mater.* **2017**, *29*, 1604856.
- [15] T. Etienne, X. Assfeld, A. Monari, *J. Chem. Theory Comput.* **2014**, *10*, 3896.
- [16] J. R. Lakowicz, *Principles of Fluorescence Spectroscopy*, Springer, New York **2006**.
- [17] Q. Peng, D. Fan, R. Duan, Y. Yi, Y. Niu, D. Wang, Z. Shuai, *J. Phys. Chem. C* **2017**, *121*, 13448.
- [18] H. Sun, Z. Hu, C. Zhong, X. Chen, Z. Sun, J.-L. Brédas, *J. Phys. Chem. Lett.* **2017**, *8*, 2393.
- [19] R. Gómez-Bombarelli, J. Aguilera-Iparraguirre, T. D. Hirzel, D. Duvenaud, D. Maclaurin, M. A. Blood-Forsythe, H. S. Chae, M. Einzinger, D.-G. Ha, T. Wu, G. Markopoulos, S. Jeon, H. Kang, H. Miyazaki, M. Numata, S. Kim, W. Huang, S. I. Hong, M. Baldo, R. P. Adams, A. Aspuru-Guzik, *Nat. Mater.* **2016**, *15*, 1120.
- [20] V. H. C. Silva, V. Aquilanti, H. C. B. de Oliveira, K. C. Mundim, *Chem. Phys. Lett.* **2013**, *590*, 201.
- [21] S. M. Menke, R. J. Holmes, *J. Phys. Chem. C* **2016**, *120*, 8502.
- [22] O. V. Mikhnenko, H. Azimi, M. Scharber, M. Morana, P. W. M. Blom, M. A. Loi, *Energy Environ. Sci.* **2012**, *5*, 6960.

- [23] R. R. Lunt, N. C. Giebink, A. A. Belak, J. B. Benziger, S. R. Forrest, *J. Appl. Phys.* **2009**, *105*, 053711.
- [24] O. V. Mikhnenko, F. Cordella, A. B. Sieval, J. C. Hummelen, P. W. M. Blom, M. A. Loi, *J. Phys. Chem. B* **2008**, *112*, 11601.
- [25] J. D. A. Lin, O. V. Mikhnenko, T. S. van der Poll, G. C. Bazan, T.-Q. Nguyen, *Adv. Mater.* **2015**, *27*, 2528.
- [26] O. V. Mikhnenko, P. W. M. Blom, T.-Q. Nguyen, *Energy Environ. Sci.* **2015**, *8*, 1867.
- [27] S. M. Menke, R. J. Holmes, *J. Mater. Chem. C* **2016**, *4*, 3437.
- [28] I. I. Fishchuk, A. Kadashchuk, L. Sudha Devi, P. Heremans, H. Bässler, A. Köhler, *Phys. Rev. B* **2008**, *78*, 045211.
- [29] T. C. Wu, D. N. Congreve, M. A. Baldo, *Appl. Phys. Lett.* **2015**, *107*, 031103.
- [30] N. Yanai, M. Kozue, S. Amemori, R. Kabe, C. Adachi, N. Kimizuka, *J. Mater. Chem. C* **2016**, *4*, 6447.
- [31] H. Nakanotani, T. Higuchi, T. Furukawa, K. Masui, K. Morimoto, M. Numata, H. Tanaka, Y. Sagara, T. Yasuda, C. Adachi, *Nat. Commun.* **2014**, *5*, 4016.
- [32] D. Zhang, L. Duan, C. Li, Y. Li, H. Li, D. Zhang, Y. Qiu, *Adv. Mater.* **2014**, *26*, 5050.
- [33] S. M. Menke, R. J. Holmes, *Energy Environ. Sci.* **2014**, *7*, 499.
- [34] A. Köhler, H. Bässler, *Electronic Processes in Organic Semiconductors: An Introduction*, Wiley-VCH, Weinheim, Germany **2015**.
- [35] A. Kretschmar, C. Patze, S. T. Schwaebel, U. H. F. Bunz, *J. Org. Chem.* **2015**, *80*, 9126.
- [36] M. J. Frisch, G. W. Trucks, H. B. Schlegel, G. E. Scuseria, M. A. Robb, J. R. Cheeseman, G. Scalmani, V. Barone, G. A. Petersson, H. Nakatsuji, X. Li, M. Caricato, A. Marenich, J. Bloino, B. G. Janesko, R. Gomperts, B. Mennucci, H. P. Hratchian, J. V. Ortiz, A. F. Izmaylov, J. L. Sonnenberg, D. Williams-Young, F. Ding, F. Lipparini, F. Egidi, J. Goings, B. Peng, A. Petrone, T. Henderson, D. Ranasinghe, V. G. Zakrzewski, J. Gao, N. Rega, G. Zheng, W. Liang, M. Hada, M. Ehara, K. Toyota, R. Fukuda, J. Hasegawa, M. Ishida, T. Nakajima, Y. Honda, O. Kitao, H. Nakai, T. Vreven, K. Throssell, J. A. Montgomery Jr., J. E. Peralta, F. Ogliaro, M. Bearpark, J. J. Heyd, E. Brothers, K. N. Kudin, V. N. Staroverov, T. Keith, R. Kobayashi, J. Normand, K. Raghavachari, A. Rendell, J. C. Burant, S. S. Iyengar, J. Tomasi, M. Cossi, J. M. Millam, M. Klene, C. Adamo, R. Cammi, J. W. Ochterski, R. L. Martin, K. Morokuma, O. Farkas, J. B. Foresman, D. J. Fox, Gaussian 09, Revision D.01, Gaussian, Inc., Wallingford, CT **2016**.
- [37] M. Moral, L. Muccioli, W.-J. Son, Y. Olivier, J. C. Sancho-García, *J. Chem. Theory Comput.* **2015**, *11*, 168.
- [38] G. te Velde, F. M. Bickelhaupt, E. J. Baerends, C. F. Guerra, S. J. A. van Gisbergen, J. G. Snijders, T. Ziegler, *J. Comput. Chem.* **2001**, *22*, 931.
- [39] C. F. Guerra, J. G. Snijders, G. te Velde, E. J. Baerends, *Theor. Chem. Acc.* **1998**, *99*, 391.
- [40] ADF 2016, SCM, Theoretical Chemistry, Vrije Universiteit, Amsterdam, The Netherlands, <http://www.scm.com> (accessed: June 2016).
- [41] E. van Lenthe, E. J. Baerends, J. G. Snijders, *J. Chem. Phys.* **1994**, *101*, 9783.
- [42] E. van Lenthe, A. Ehlers, E.-J. Baerends, *J. Chem. Phys.* **1999**, *110*, 8943.